Journal of Materials Chemistry C

Extrinsic doping of Hg_2GeTe_4 in the face of defect compensation and phase competition

Journal:	*Journal of Materials Chemistry C*
Manuscript ID	TC-ART-01-2023-000209.R1
Article Type:	Paper
Date Submitted by the Author:	28-Apr-2023
Complete List of Authors:	Porter, Claire; Colorado School of Mines, Materials Science Qu, Jiaxing; University of Illinois at Urbana-Champaign, Ciesielski, Kamil; Colorado School of Mines, Physics Ertekin, Elif; University of Illinois, Department of Mechanical Science and Engineering Toberer, Eric; Colorado School of Mines,

Journal Name

ARTICLE TYPE

Cite this: DOI: 10.1039/xxxxxxxxxx

Extrinsic doping of Hg_2GeTe_4 in the face of defect compensation and phase competition

Claire E. Porter,[a,*] Jiaxing Qu,[b,*] Kamil M. Cielsielski,[a] Elif Ertekin,[b] and Eric S. Toberer[a]

Received Date
Accepted Date

DOI: 10.1039/xxxxxxxxxx

www.rsc.org/journalname

Emerging semiconductors for energy and information applications increasingly consist of compounds with much higher structural and chemical complexity than their unary and binary predecessors. Often, such complexity has limited the ultimate potential of new materials due to challenges with carrier concentration control in the face of native defects. For example, native defects in ordered vacancy compound Hg_2GeTe_4 impose challenging requirements for extrinsic doping to achieve carrier concentration levels suitable for thermoelectric performance. Here, we address this challenge by performing first-principles defect analysis on 16 extrinsic dopants under different synthetic conditions in Hg_2GeTe_4. Eight of these dopants (Au, Ag, Cu, Li, In, Ga, Zn, Sc) are predicted to tune the carrier concentration over three orders of magnitude. The remaining eight dopants (Na, Mg, Y, La, Sb, Bi, Br, I) have high formation energy and are predicted to have minimal impact. Samples with the eight most promising dopants were synthesized from elemental precursors and their transport property measurements are in excellent agreement with predicted values. Consistent with theory, degenerate n-type doping proves to be unavailable and extrinsic compensating defects are understood to be the primary barrier. The p-type dopants were found to be effective; we obtained degenerate carrier concentration with Ag and decent thermoelectric performance (zT = 0.4 at 473 K). Shifting the Fermi level to the valence band edge reduces the concentration of V_{Hg}^{-2} and associated ionized defect scattering. Such observations highlight the interwoven network of dependencies when doping multinary semiconductors, and emphasize the importance of theory-experimental collaborations when exploring new materials.

Introduction

Control of the charge carrier concentration is a vital aspect of new semiconductor development.[1–5] Such materials form the basis of new energy conversion and storage devices, including photovoltaics[6], thermoelectrics[7], and batteries[8,9] etc. As interest in increasingly exotic semiconductors grows, doping has become a persistent challenge, especially for complex structures. For instance, the photovoltaic semiconductor Cu_2ZnSnS_4 (CZTS) has been notoriously challenging to dope due to high concentrations of native antisite defects (Cu_{Zn}^{-1}) arising from the energy proximity of stannite and kesterite quarternary diamond-like structures .[10] Generally, structural complexity introduces (*i*) more synthetic degrees of freedom, (*ii*) an abundance of sites for native defects or extrinsic dopants (including multiple vacancies, interstitials, and antisite defects), and (*iii*) additional competing phases. Therefore, rationally doping exotic semiconductors in complex structures to optimal carrier concentrations by chemical intuition alone is often a fraught process.

The emergence of defect theory in concert with first-principles calculations now enables the prediction of defect formation energies in a candidate material.[11–13] After decades of effort in improving simulation methods, computation is increasingly accurate at predicting important transport phenomena and material dopability.[12] Beyond ex post facto explanations of prior experimental results[14,15], such calculations can guide experimental campaigns. Examples where theory has guided experiment include the unusual n-type Zintl compound $KGaSb_4$ and n-type doping of Mg_3Sb_2 under Mg-rich conditions, formerly thought to be unachievable.[16,17] Yet in spite of the well-established predictive capability of first-principles approaches, theory-driven experiments to optimize carrier concentrations remain rare. This is likely due

* equal contributions
[a]*University of Illinois at Urbana-Champaign, Urbana, IL 61801.* [b]*Colorado School of Mines, Golden, CO 80401.* [c]*Northwestern University, Evanston, IL 60208.* [d]*University of California Santa Barbara, Santa Barbara, CA 93106. E-mail: c7porter@gmail.com, jiaxing6@illinois.edu*
† Electronic Supplementary Information (ESI) available

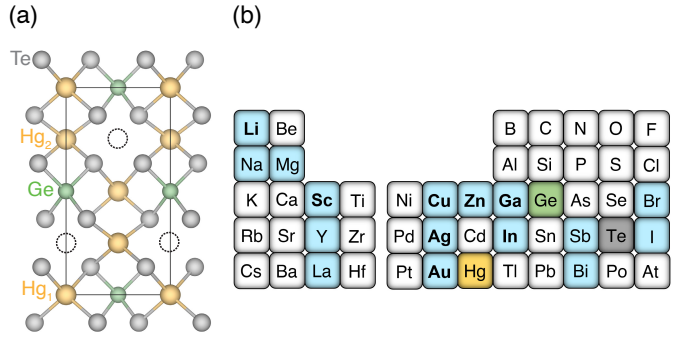

Fig. 1 (a) Hg_2GeTe_4 crystallizes in the defect chalcopyrite structure (space group *I-4*), characterized by ordered vacancy sites (empty circles). The unique Hg Wyckoff sites are labeled and appear in subsequent defect diagrams. (b) Extrinsic dopants spanning a wide range of electronegativites were interrogated computationally (blue); the bolded elements designate dopants that were predicted to form low energy defects in Hg_2GeTe_4.

to the fact that these types of simulations have historically been computationally expensive and due to the difficulty in connecting computational conditions (e.g. elemental chemical potentials) with experimental observables. However, if experimental doping efforts can be guided by theory the benefits are clear. For example, if carrier concentrations in a target semiconductor are observed to be too low in experiment, it can be difficult to know whether synthetic conditions should be further optimized, if alternative dopants should be selected, or if the semiconductor simply cannot be doped to the desired degree. Computation-guided experiment provides strategies to achieve desired carrier concentrations from the outset by identifying killer defects and selecting optimal growth conditions; if a semiconductor simply cannot be doped it helps save wasted time and effort.

Hg_2GeTe_4 provides an intriguing platform for studying defects in terms of crystal chemistry and native defects. The presence of divalent (Hg) and tetravalent (Ge) cations provides competing sites for extrinsic dopants. Structurally, Hg_2GeTe_4 is a defect chalcopyrite derived from two stacked zinc blende cells containing an ordered vacancy site (depicted as dashed circles in Figure 1). This chemical and structural complexity offers a compelling test bed beyond simple binary compounds. Undoped Hg_2GeTe_4 is experimentally found to posses a carrier concentration of $0.5–1\times10^{18}$ h^+ cm^{-3} depending on growth conditions.[5] Beyond serving as a model system, Hg_2GeTe_4 is also a candidate thermoelectric material with ultra-low thermal conductivity (<0.60 W/m-K at 200°C) and excellent *p*-type mobility (>60 cm^2/Vs at 200°C)[5,18]. First-principles calculations indicate that the conduction band is much lighter than the valence band ($m^*_{DOS,CB}/m^*_{DOS,VB} = 0.053$), which suggests that *n*-type electronic mobility would be exceptional.

In this work, we consider Hg_2GeTe_4 as a model material to study the doping challenges and mechanisms in a relatively structurally complex semiconductor. Diamond-like semiconductors are an excellent model system choice due to their chemical breadth and high predicted thermoelectric and photovoltaic properties.[19–21] Chemically complex diamond-like semiconductors such as $Cu_2HgGeTe_4$ are predicted to posses excellent n-type thermoelectric properties[18], but are unable to be doped *n*-type due to low energy Cu^{-1}_{Hg} and V^{-2}_{Cu} defects.[5] This doping asymmetry is common among DLS compounds.[19,22] On the other hand, Hg_2GeTe_4 may be doped *p* or *n*-type due to sufficiently high energy V^{-2}_{Hg} defects.[5] This work builds on our previous investigation of the native defects of Hg_2GeTe_4 using the phase boundary mapping technique.[5] We consider 16 different extrinsic dopants and conduct transport measurements on those expected to increase as well as decrease the carrier concentration to provide validation to our calculations and to assess their potential limitations. The eight dopants with the lowest energy defects (Ag, Li, Au, Cu, Sc, Ga, Zn, In; Fig 1b) are the focus of this study. We analyze different sources of limitations in doping which will help with understanding and overcoming doping challenges in functional materials beyond Hg_2GeTe_4.

Results & Discussion

1 Computational prediction

To fully explore potential candidates for doping Hg_2GeTe_4 to high *n*- and *p*-type carrier concentrations, we surveyed a comprehensive suite of 16 dopants. The 16-dopant suite consists of alkali and alkaline earth metals (Li, Na, Mg), rare earth (Sc, Y, La), coinage metals (Cu, Ag, Au), semi-metals (In, Ga, Zn) as well as pnictogens (Sb, Bi) and halogens (Br, I). We considered elements across a broad range of electronegativities to reduce bias in our dopant selection and encourage multiple types of defects (i.e. allow for cation or anion substitutional defects). We employ phase boundary mapping[17,18] to determine the full range of carrier concentrations achievable across the phase stability region of Hg_2GeTe_4 (Figure 2a) under extrinsic doping.

1.1 Phase Boundary Mapping

Phase boundary mapping is a technique to explore the chemical potential limits of a target compound across its entire stability region. Figure 2a shows from our previous work that the chemical potential of Hg_2GeTe_4 is limited by the formation of HgTe (under Hg-rich conditions), GeTe (under Ge-rich conditions) and Te (under Te-rich conditions).[5] These competing phases restrict the phase stability of Hg_2GeTe_4 to a polygon in chemical potential space (Figure 2a). Taking the point labeled "Hg-poor/Ge-rich" as an example, Hg_2GeTe_4 can be grown in sufficiently Hg poor conditions until the Hg_2GeTe_4 crystal lattice becomes unstable with respect to formation of GeTe and Te. Critically, the scarcity or prevalence of Hg in the thermodynamic environment influences defect formation – when Hg is scarce, V^{-2}_{Hg} native defects are encouraged and Hg^{+2}_i are suppressed by the decreased chemical potential of mercury. Conversely, when Hg is abundant, the chemical potential of Hg is increased and Hg^{+2}_i forms readily and V^{-2}_{Hg} are suppressed.

We found previously that the native *p*-type nature of Hg_2GeTe_4 arises primarily from low energy V^{-2}_{Hg} native defects.[5] Consequently, the range of native carrier concentration can be tuned by the chemical potential of Hg under different growth conditions; the highest computationally predicted carrier concentra-

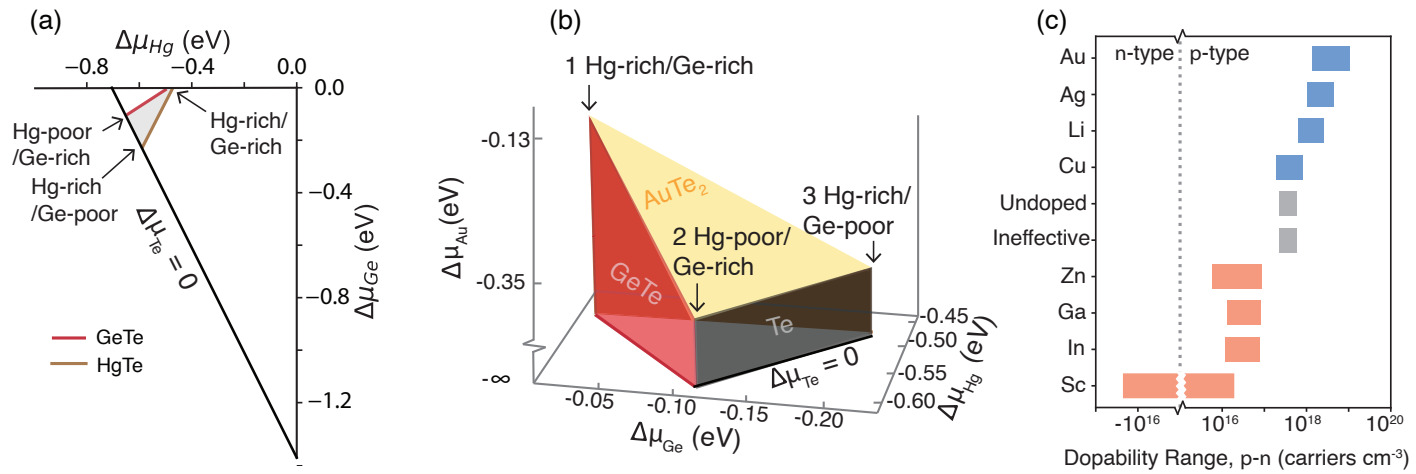

Fig. 2 (a) The phase stability of Hg_2GeTe_4 is bounded by the competing phases HgTe, GeTe, and Te.[5] (b) When we introduce an extrinsic dopant (e.g. Au), the new chemical species adds a dimension to the phase stability area for Hg_2GeTe_4. The yellow slanted triangle shows the boundary with $AuTe_2$, which limits the dopant solubility of Au in Hg_2GeTe_4. The vertices are invariant points associated with the presence of four phases. (c) The undoped carrier concentration (grey) is predicted to be lowest under Hg-rich/Ge-rich growth conditions (2.2×10^{17} h^+ cm^{-3}) and highest under Hg-poor/Ge-rich conditions (5.9×10^{17} holes cm^{-3}). A subset of candidate dopants are predicted to either increase (blue) or decrease (salmon) the carrier concentration of Hg_2GeTe_4; again, the carrier concentration range arises from different growth conditions. Ineffective dopants Na, Mg, Y, La, Sb, Bi, Br, and I do not shift the carrier concentration.

tion in undoped material (5.9×10^{17} h^+ cm^{-3}) is achieved under Hg-poor/Ge-rich conditions where V_{Hg}^{-2} have the lowest defect formation energy, and the lowest predicted carrier concentration (2.2×10^{17} h^+ cm^{-3}) occurs under Hg-rich/Ge-rich conditions where V_{Hg}^{-2} are suppressed.

Extrinsically doping Hg_2GeTe_4 adds another chemical dimension by the introduction of a fourth element, creating the phase stability volume in Figure 2b. The z-axis in Figure 2b is the chemical potential of the dopant Au ($\Delta\mu_{Au}$). The triangle of Figure 2a is extruded from $\Delta\mu_D = -\infty$ to higher dopant concentrations, forming the 3D triangular prism in Figure 2b. The maximum height of this prism is bound by dopant-limiting phase $AuTe_2$, which is listed in Table 1 as $\Delta\mu_D$ = -0.35 eV under 2 Hg-poor/Ge-rich conditions or -0.13 eV under 1 Hg-rich/Ge-rich conditions. Since the degree to which a dopant is incorporated correlates with its chemical potential, finding dopants that allow the triangular prism in Figure 2b to grow tall is desirable. Dopant-containing competing phases (Table 1) limit the solubility and therefore the maximum carrier concentration achieved by a given chemical species.

1.2 Extrinsic Dopants

To begin exploring extrinsic dopants, we consider the characteristics of an ideal dopant. An ideal dopant has high solubility in the parent compound, one type of defect dominates (either donor, or acceptor, but not both), and dopant defects are lower in energy at the equilibrium Fermi level than native defects. Dopant solubility is governed by both allowed chemical potential (thermodynamics) and the energy cost of perturbing the host crystal to form the defect. Assuming a dopant can dissolve easily into the lattice, its ability to form one majority type defect (donor or acceptor) is desirable to avoid compensation. Additionally, these extrinsic defects should be lower in energy than native defects

	$\Delta\mu_D$, 1	$\Delta\mu_D$, 2	Competing phase
Sb	-0.10	-0.27	Sb_2Te_3
Au	**-0.13**	**-0.35**	**$AuTe_2$**
Ag	**-0.19**	**-0.26**	**AgTe**
Bi	-0.43	-0.60	Bi_2Te_3
Cu	**-0.48**	**-0.56**	**$Cu_2HgGeTe_4$***
Ga	**-0.97**	**-1.11**	**$HgGa_2Te_4$**
In	**-1.01**	**-1.15**	**$HgIn_2Te_4$**
Zn	**-1.12**	**-1.21**	**ZnTe**
Li	**-1.99**	**-2.05**	**Li_2Te**
Sc	**-2.54**	**-2.65**	**ScTe**
Mg	-2.83	-2.94	MgTe
Br	-3.20	-3.10	Hg_3Br_4Te
Na	-3.47	-3.81	$NaTe_3$
I	-3.94	-3.80	$Hg_3I_2Te_2$
La	-4.11	-4.26	La_3Te_4
Y	-4.93	-5.10	Y_2Te_3

Table 1 The maximum dopant chemical potential ($\Delta\mu_D$, eV/atom) is slightly more favorable under 1, Hg-rich/Ge-rich growth conditions versus 2, Hg-poor/Ge-rich conditions, with the exception of the halogens. For each dopant, a singular competing phase limits dopant chemical potential regardless of the growth conditions. The dopants that form defects $<$ 1 eV at E_F = 0.24 eV are listed in bold. *$Cu_2HgGeTe_4$ is known to form a full solid solution with Hg_2GeTe_4.[5,18,23]

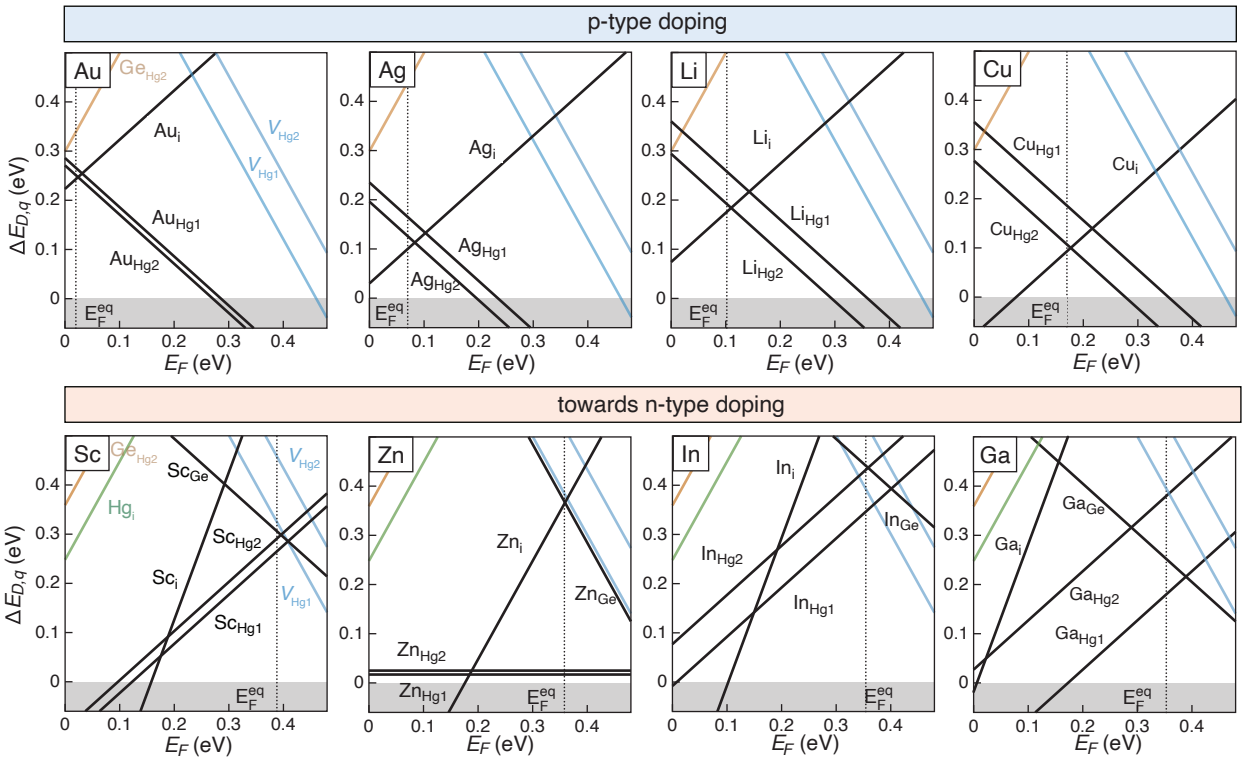

Fig. 3 For each extrinsic dopant, a doping type (n or p) was determined to be the most impactful; the associated defect diagram under the requisite elemental chemical potentials are show. For p-type doping (upper row), Hg-poor/Ge-rich conditions facilitate substitution on the Hg site. Conversely, n-type doping favors Hg-rich/Ge-rich conditions to raise the energy of V_{Hg}^{-2}. Both rows present dopants in decreasing order of effectiveness at altering the carrier concentration. The equilibrium Fermi energy E_F^{eq} (marked by the dashed grey line) is pinned around the intersection of lowest energy defects.

The undoped equilibrium E_F^{eq} is 0.19 eV when Hg-poor/Ge-rich or 0.24 eV when Hg-rich/Ge-rich.[5] The E_F^{eq} associated with equal populations of n and p ($n = p = 2.7 \times 10^{16}$ carriers cm^{-3}) in Hg_2GeTe_4 is 0.37 eV.

to generate sufficient free charge carriers to influence transport. In Hg_2GeTe_4, native defects are sufficiently high in energy to offer modest p and n-type "dopability windows" of $\Delta E_p = 0.25$ eV and $\Delta E_n = 0.14$ eV,[5] where ΔE_p refers to the intersection of the lowest energy native donor at the valence band maximum, and ΔE_n refers to the intersection of the lowest energy acceptor defect with the conduction band minimum.[22]

Of the 16 dopants considered, eight are predicted to significantly affect the carrier concentration under optimal growth conditions (Au, Ag, Li, Cu, Zn, Ga, In, Sc; Figure 2c). Four dopants (blue) increase the carrier concentration above undoped levels (grey); conversely the four dopants that lower the hole carrier concentration are shown in orange. The doped carrier concentration was calculated at the three invariant points (Figure 2b); the maximum and minimum values set the range of carrier concentration achieved by each dopant in Figure 2c. The dopants Na, Mg, Y, La, Br, I, Sb, Bi, (grey) are found to be ineffective at changing the carrier concentration beyond the undoped range.

Finally, we consider the validity of the rigid band approximation with respect to doping (Figure S1). Analysis of the supercell density-of-states for the lowest energy defects at the corresponding charge state results in minimal changes in the DOS near the band edges and the absence of charge transition levels in the gap. As such, we utilize the undoped effective mass and band gap values to calculate the carrier concentration for the 16 dopants.

Successful p-type dopants: Au, Ag The highest predicted carrier concentrations in Hg_2GeTe_4 are achieved via doping with Au and Ag (Figure 2c). Our defect calculations show that the main acceptor defect driving the degenerate p-type transport is D_{Hg}^{-1} (D = Au, Ag), as shown in Figure 3 (under Hg-poor/Ge-rich growth conditions). Au and Ag extrinsic acceptor defects nearly push the equilibrium Fermi level to the valence band (Figure 3), resulting in high p-type carrier concentrations. Note that E_F^{eq} is pinned around the intersection of lowest energy donor and acceptor defects, with a slight offset from the intersection point for all defect diagrams in Figure 3. While such offsets can arise from contributions of thermally excited carriers[24], the offset to the left here instead arises from asymmetry in the band effective masses of holes and electrons[5], i.e. larger valence band effective mass than conduction band. This self-regulation effect can be visualized in Figure S12, which shows the defect diagrams but also includes virtual band-edge 'defect' holes arising from considering the conduction band as a deep acceptor with charge transition level at the CBM[24]. Moreover, both dopants benefit from Hg-poor/Ge-rich growth conditions, which encourage the formation of the acceptor defect D_{Hg}^{-1}. Under these conditions, Au-doping achieves an exceptional predicted carrier concentration of 1.1×10^{19} h$^+$ cm^{-3},

and Ag-doping results in a carrier concentration of 4.5×10^{18} h^+ cm^{-3}.

Importantly, for both dopants the antisite defect D_{Hg}^{-1} is sufficiently low energy that native defects only play a minor role (Figure 3). Additionally, the competing interstitial defect D_i^{+1} is high enough in energy (especially for Au) that degenerate *p*-type behavior is achieved. Note that this site is the ordered vacancy site (empty circles in Figure 1) and not the traditional interstitial sites of diamond-like semiconductors. Finally, we note that even under Hg-rich/Ge-rich conditions, Au and Ag still increase the hole concentration of Hg_2GeTe_4 above undoped levels (Figure 2c), but their impact is reduced due to the increased compensation between D_{Hg}^{-1} and D_i^{+1} (Au: 1.3×10^{18} h^+ cm^{-3}, Ag: 1.1×10^{18} h^+ cm^{-3}; (see defect diagram under Hg-rich/Ge-rich growth conditions in Figure S2)

Limited by defect compensation: Cu, Li Similar to Au and Ag, doping with Cu or Li improves the carrier concentration of Hg_2GeTe_4 under Hg-poor/Ge-rich growth conditions. However, Cu and Li are less effective dopants than the heavier noble metals due to increased compensation by donor defect D_i^{+1} (D = Li, Cu). Inspection of Figure 3 reveals that the the relative energy of the D_i^{+1} substitutional defect to the D_{Hg}^{-1} interstitial defect determines the effectiveness of a *p*-type dopant in this system. For Li and Cu, the interstitial defect is low enough in energy to significantly compensate the Hg substitutional defect and high *p*-type concentrations are thus unachievable. Carrier concentrations of 2.6×10^{18} and 8.0×10^{17} h^+ cm^{-3} are the maximum calculated carrier concentrations for Li and Cu, respectively. Recall that the maximum carrier concentration for undoped Hg_2GeTe_4 is 5.9×10^{17} h^+ cm^{-3} from theory.

Non-Hg-poor/Ge-rich growth conditions render the defect compensation even worse for Li and Cu. Under Hg-rich/Ge-rich and Ge-poor conditions, the D_{Hg}^{-1} defect rises in energy, leading to increased compensation by interstitial defect D_i^{+1} and a lower carrier concentration. Hg-rich/Ge-rich conditions in particular also increase the chemical potential of Li and Cu and thus lower the energy of donor D_i^{+1}. These combined effects lead to a reduction in carrier concentration of approximately 1 order of magnitude compared to the Hg-poor/Ge-rich conditions for both Li and Cu (Figure 2c). Hence, Li and Cu are promising *p*-type dopants only under Hg-poor/Ge-rich conditions, and are not as effective as Au and Ag. This compensation by the interstitial defect may be more pronounced for Li and Cu due to their smaller ionic radii and their relative ease at forming interstitial defects. Interestingly, Cu has a much greater chemical potential than Li (Table 1) however Li is a slightly more effective *p*-type dopant than Cu. Li doping achieves higher carrier concentration than Cu doping (Figure 2c) or synonomously the equilibrium E_F achieved by Li doping is closer to the valence band than it is for Cu. It appears that Li has overcome its chemical potential limitations and readily forms both interstitial defects and perhaps more surprisingly due to its size, Hg antisite defects.

Towards *n*-type doping: Sc, Zn, In, Ga We know from our previous work that Hg_2GeTe_4 possesses an *n*-type dopability window, so in this work we sought to identify dopants that would achieve majority electron carrier concentrations. The ideal *n*-type dopant would have low enough energy donor defect(s) to introduce large populations of electrons that exceed the hole concentration in native *p*-type Hg_2GeTe_4. We note that due to the band mass discrepancy in this material highlighted in the Introduction, the E_F associated with equal populations of *n* and *p* is E_F = 0.37 eV, rather than the midgap value of 0.24 eV (DFT bandgap is 0.48 eV[5]). The four dopants that reduce the hole concentration of Hg_2GeTe_4 below undoped levels are depicted by orange bars in Figure 2c and constitute the bottom row of Figure 3.

These dopants (Sc, Zn, Ga, In) generate both donor (interstitial and Hg antisite) and acceptor (Ge antisite) defects (Figure 2). This leads to significant compensation and prevents a single carrier type from dominating and yielding high carrier concentration. In contrast to the previously discussed *p*-type dopants, Hg antisite defects are donor defects for these trivalent cations. The Ge substitutional site is the acceptor (Figure 3).

In the case of the trivalent dopants (D = Sc, Ga, In), the compensation arises from antisite defects D_{Hg}^{+1} and D_{Ge}^{-1}, and the ever-present native defect V_{Hg}^{-2}. For example, indium-doped Hg_2GeTe_4 is heavily compensated with a hole concentration of 3.3×10^{16} and an electron concentration of 2.1×10^{16} carriers cm^{-3} under the most favorable *n*-type doping synthetic conditions (Hg-rich/Ge-rich). Considering Figure 2c, we observe that Sc can dope Hg_2GeTe_4 either *p* or *n*-type depending on growth condition, albeit to low carrier concentrations. The predicted E_F range is within ±0.02eV of the E_F associated with equal populations of electron and holes (i.e., $n = p$); as such, bipolar behavior is likely.

Moving on to divalent Zn, we observe different behavior than found in trivalent In, Ga, or Sc. Dopant compensation now arises from the competing nature of antisite defect Zn_{Ge}^{-2} and interstitial Zn_i^{+2}. Further, Zn_{Hg}^{0} forms as an extremely high concentration charge-neutral defect. The low energy of Zn_{Hg}^{0} indicates alloying at concentrations beyond the isolated defects modeled herein. Indeed, this high solubility is consistent with the established pseudobinary between ZnTe-HgTe; these binaries both adopt the zinc blende structure (from which defect chalcopyrite is derived) and share a full solid solution at moderate temperatures.[25,26]

In summary, Sc, Zn, Ga, and In form multiple low energy defects (Figure 3) that are compensatory in nature and prevent tuning the carrier concentration to high levels. With these dopants, the undoped Fermi level at 0.24 eV under Hg-rich/Ge-rich conditions is shifted towards the conduction band from 0.35 to 0.39 eV. As such, these four dopants are predicted to lower the hole carrier concentration of Hg_2GeTe_4 by one order of magnitude from undoped levels (Figure 2c).

High energy defects: Na, Mg, Y, La, Br, I, Sb, Bi The final eight surveyed dopants are ineffective at changing the carrier concentration in Hg_2GeTe_4 due to high energy defects. Their resulting ineffectiveness at influencing transport is depicted in Figure 2c and Table S1 where the carrier concentration of Hg_2GeTe_4 is unchanged by introduction of these dopants. For most of these elements, the dopant chemical potential is strongly restricted by a dopant-containing competing phase (Table 1). For example, with Na-doping, $NaTe_3$ limits the maximum chemical potential of

sodium ($\Delta\mu_{Na}$ ranges from -3.47 to -3.81 eV/atom) at the invariant points. This increases the formation energy of Na defects. The lowest energy defects are still high: antisite defect Na_{Hg}^{-1} occurs at energies ranging from 2.1–2.6 eV depending on the Hg chemical potential. This generates defect concentrations on the order of 10^3 defects per cm^3, which is trivial compared with intrinsic concentrations (on the order of 10^{17} carriers/cm^3).

Alkali earth, rare-earth, and halogen elements behave similarly to Na and form high energy defects that are unlikely to influence transport. While La is known as a filler in $CoSb_3$ skudderudites[27], La interstitials are very high energy in Hg_2GeTe_4, likely due to the much smaller void volume. The void center to nearest neighbor distance is 2.33 Å for $Hg_2GeTe_4$and 3.35 Å for $CoSb_3$. All of these dopants are ineffective due to a low dopant elemental chemical potential (Table 1).

Finally, pnictogens, unlike the previously discussed dopants, experience limited solubility that cannot be entirely attributed to reduced chemical potential. The chemical potential of $\Delta\mu_{Bi}$ is -0.4 and that of Sb is -0.1 eV, which is higher than most of our dopants (Table 1). It is therefore likely that the insolubility of these dopants is due to local strain or Coulombic repulsion generated by the defect, rather than chemical potential limits. This is somewhat surprising as Sb and Bi are known p-type dopants in CdTe.

1.2.1 Doping efficiency

From a synthetic perspective, it is valuable to understand the fraction of dopant atoms that contribute to the desired doping effect. Here, we focus on Cu, Li, Ag, and Au for *p*-type doping. For these dopants, the chemical doping efficiency is given by:

$$\eta = \frac{[X_{Hg1}] + [X_{Hg2}]}{[X_{Hg1}] + [X_{Hg2}] + [X_i]} \quad (1)$$

The numerator and denominator are the dopant acceptor and total dopant defect concentrations, respectively. Here, the concentrations of each defect N are:

$$[N] = [N_{site}] exp(\frac{-\Delta E_{D,q}}{k_B T}) \quad (2)$$

where $\Delta E_{D,q}$ refers to the defect formation energy at a given equilibrium Fermi level, k_B refers to the Boltzman constant, N_{site} is site concentration in the host crystal, and $T = 673$ K was chosen, consistent with the temperature used in charge neutrality and defect calculations (see Methods). For Cu, Li, and Ag, the doping efficiency is ∼50% (Table S2) as such the charge neutrality equations simplifies to $[A] \approx [D]$. In contrast, Au as a dopant leads to 61% doping efficiency under Hg-poor/Ge-rich conditions and an 84% efficiency under Hg-rich/Ge-rich conditions. While the doping efficiency under Hg-rich/Ge-rich conditions is greater for Au, the acceptor defects are higher in energy and ultimately we see lower hole carrier concentration for Hg-rich/Ge-rich conditions.

While In, Sc, Zn, and Ga are not predicted to be effective *n*-type dopants (Figure 2), they nevertheless move the Fermi level towards the conduction band (Figure 3). Inspection of Figure 3 indicates that In, Sc, and Ga should have high doping efficiency due to the low energy of the D_{Hg1}^{+1} site. However, it is notable that Zn should have extremely low doping efficiency (0.1%) due to the high probability of Zn residing on the Hg sites (charge neutral).

2 Experimental Section

2.1 Synthesis and structural characterization

Bulk polycrystalline samples of Hg_2GeTe_4 were prepared with the promising (Ag & Au) dopants and the compensated (Cu, Ga, In, Sc, Zn) species discussed above. No samples were synthesized with Li given its high reactivity with mercury[28] and our desire to minimize our exposure to highly toxic compounds. To screen the dopants, we prepared samples with stoichiometries where we removed 0.07 Hg per formula unit and added 0.07 dopant per formula unit (i.e. $Hg_{1.93}GeTe_4D_{0.07}$) except Zn and Ga, which used 0.05. This was to encourage Hg-antisite defects, which are beneficial for both *p*-type and *n*-type doping (Figure 3). Additional samples were prepared to explore changes in electronic properties as a function of growth condition, particularly for Au and Ag doping, see Table 2 for specific compositions.

Density and SEM Density measurements found values above 98% of the calculated value for all samples, consistent with scanning electron microscopy (SEM) imaging which showed very little porosity. SEM images of the microstructure for the extrinsically doped samples are presented in Supplemental Figures S3-S7. SEM revealed trace impurity phases that had grain sizes between 1-10 μm. The combination of high sample density and significant grain sizes indicates that annealing for >50 hr at high temperature (350°C) and pressing (> 6 hrs at 40 MPa) led to significant diffusion and suggests that samples were close to equilibrium.

XRD Each sample was checked for majority phase content (Hg_2GeTe_4) and any impurity phases via a combination of SEM, energy dispersive spectroscopy (EDS), and X-ray diffraction (XRD), as described in Methods. The particular impurity phases present (in trace amounts) pin the sample to a point in chemical space (Figure 2b). Rietveld refinement was performed using the TOPAS academic software[29], and impurity phase content was refined. The maximum weight percent of impurity phase observed across all samples was 4 wt% Te, 3 wt% GeTe, and 8 wt% HgTe. Samples that generated higher impurity phase content than these percentages were discarded from the study. XRD patterns are shown in Supplement (Figures S3 - S7).

Dopant alloying in secondary phases While we successfully observed the native secondary phases (GeTe and HgTe or Te), we rarely saw the predicted dopant-containing phase due to alloying between the dopant and one of the secondary phases (Figures S3-S7). We chose stoichiometries (Table 2) with sufficient dopant to saturate the crystal with extrinsic defects. Under such dopant-rich conditions, we expect to see the dopant-containing phases are listed in Table 1. However, the only dopant we observed in experiment to generate the expected dopant-containing secondary phase was Au, which precipitated $AuTe_2$, observable in XRD and SEM (Figure S3). For all other dopants, we either observed an unreported compound (e.g., $Ag_{1.17}Hg_{1.5}Ge_{1.17}Te_4$, Figure S4) or no dopant-containing phase was detected in SEM or XRD (Fig-

Dopant	Stoichiometry	Impurity Phases	Synthetic regime	n_H (10^{18} cm^{-3})	wt% HgTe
Ag	$Hg_{1.93}GeTe_4Ag_{0.07}$	HgTe, GeTe	Hg-rich/Ge-rich	12	0.1
	$Hg_2GeTe_4Ag_{0.07}$	HgTe, GeTe, quaternary	Hg-rich/Ge-rich	10	0.4
	$Hg_{1.965}GeTe_4Ag_{0.035}$	GeTe, Te	Hg-poor/Ge-rich	12	0.0
	$Hg_{1.79}Ge_{1.07}Te_4Ag_{0.07}$	GeTe, Te	Hg-poor/Ge-rich	16	0.0
Au	$Hg_{1.93}GeTe_4Au_{0.07}$	GeTe, HgTe, $AuTe_2$	Hg-rich/Ge-rich	3.0	0.1
	$Hg_{1.965}GeTe_4Au_{0.035}$	GeTe, Te, $AuTe_2$	Hg-poor/Ge-rich	6.8	0.0
	$Hg_{1.79}Ge_{1.07}Te_4Au_{0.07}$	GeTe, Te, $AuTe_2$	Hg-poor/Ge-rich	7.7	0.0
Cu	$Hg_{1.93}GeTe_4Cu_{0.07}$	GeTe, Te	Hg-poor/Ge-rich	1.1	0.0
	$Hg_{1.965}GeTe_4Cu_{0.035}$	GeTe, Te	Hg-poor/Ge-rich	0.7	0.0
In	$Hg_{1.93}GeTe_4In_{0.07}$	HgTe, GeTe	Hg-rich/Ge-rich	0.24	7.7
Sc	$Hg_{1.93}GeTe_4Sc_{0.07}$	HgTe, GeTe	Hg-rich/Ge-rich	0.27	1.9
	$Hg_2GeTe_4Sc_{0.05}$	HgTe, GeTe	Hg-rich/Ge-rich	1.6*	7.4
Zn	$Hg_{1.95}GeTe_4Zn_{0.05}$	HgTe, GeTe	Hg-rich/Ge-rich	0.30	1.9
	$Hg_2GeTe_4Zn_{0.05}$	HgTe, GeTe	Hg-rich/Ge-rich	0.24	2.8
	$Hg_2GeTe_4Zn_{0.07}$	HgTe, GeTe	Hg-rich/Ge-rich	0.88*	5.7
Ga	$Hg_{1.90}GeTe_4Ga_{0.05}$	GeTe, Te	Hg-poor/Ge-rich	3.3	0.0
	$Hg_2GeTe_4Ga_{0.05}$	HgTe, GeTe	Hg-rich/Ge-rich	-1.2*	6.7

Table 2 The nominal stoichiometries for all synthesized samples are tabulated by dopant; $Hg_{1.93}GeTe_4D_{0.07}$ was generally chosen as the starting stoichiometry. To determine the synthetic regime for each sample, the impurity phases were determined via SEM/EDS. The measured Hall carrier concentration at 200°C is highest for Ag-doping, demonstrating successful p-type doping. Several samples (doped with Zn, Sc, Zn) have bipolar carrier concentration, designated with a (*). Temperature-dependent transport data for samples are show in Figure 5 (Au, Ag), Figure S8 (Cu), Figure 6 (In, Sc, Zn) & S10 (bipolar Zn and Sc samples), and Figure S9 (p-type Ga). Weight percentage of competing secondary phases was determined via Rietveld refinement and found to be less than 4% for GeTe, Te, and $AuTe_2$. HgTe wt% was higher and is listed in the last column of this table. R_{wp} ranges from 30 – 51% and χ^2 ranges from 1.2 – 1.7.

ures S5-S7) and the dopant was detected via EDS to be alloyed into HgTe or GeTe.

For Sc doping, small inclusions of average stoichiometry $Sc_{19}Ge_{19}Te_{58}Hg_4$ (averaged from 7 separate EDS measurements on different inclusions; population standard deviation $\leq 3\sigma$) were observed in Sc-doped samples (Figure S6-S7). It is known that the solubility of Sc in GeTe is quite low; the observed phase may be thermodynamically stable.[30] Alloying behavior was expected with Cu-doping due to the established full solid solution between $Cu_2HgGeTe_4$ and Hg_2GeTe_4.[5,18,23] In and Zn were found alloyed into HgTe (10-12 at% In in HgTe, 8-35 at% Zn in HgTe), which is expected from their known solubility in this compound.[26,31] Ga was observed alloyed into HgTe and GeTe (2-3 at% in each) which is expected given its small solubility with both compounds.[32,33] This alloying (Figure S5-S7) impacts the defect calculations performed above in the following way: alloying of secondary phases expands their single phase region in chemical potential space and thus decreases the Hg_2GeTe_4 single phase region. This can be a source of offset between predicted carrier concentration and measured values. The impact of alloying on the chemical potential space can be addressed by calculating the enthalpy of mixing, but this is not a common procedure when considering the dopability of semiconductors.

2.2 Transport measurements

Room temperature Seebeck coefficient and Hall carrier concentration were measured on samples doped with Cu, Ag, Au, Sc, In, Zn, and Ga. Negative or bipolar Hall data were observed in a few samples doped with Ga, Sc, and Zn ($Hg_2GeTe_4Sc_{0.05}$, $Hg_2GeTe_4Zn_{0.05}$, and $Hg_2GeTe_4Ga_{0.05}$, Table 2, Figure S10). It is likely that this bipolar behavior is due higher HgTe content arising from stoichiometries that inadvertently generated excess HgTe, which is known to have exceptionally mobile electrons ($\mu > 5{,}000$ cm^2 V^{-1}s^{-1}, Figure S11).[34] Removing Hg from the formula Hg_2GeTe_4 is therefore crucial for good quality samples and to avoid composite effects. Interestingly, Ag seems to avoid this problem ($Hg_2GeTe_4Ag_{0.07}$ has $<$ 1 wt% HgTe, Table 2). Since samples with negative Hall and positive Seebeck coefficient data are clearly exhibiting bipolar electronic conduction, we discarded them (3 total) from the main study and their data are plotted and discussed separately in Figures S10.

The resulting Seebeck coefficient and Hall carrier data are plotted in Figure 4, along with the theoretical α vs n_H curve calculated using the classic single parabolic band (SPB) model to analyze the effective band structure of Hg_2GeTe_4. The valence band effective mass $m^*_{DOS} = 0.17m_e$ is calculated from these experimental data using the SPB model and assuming that electrons are mainly scattered via ionized defects near room temperature.[35] We choose this scattering regime based on prior scattering decomposed carrier transport calculations in Hg_2GeTe_4[5] as well as the experimental observation of mobility increasing with temperature in our undoped and most of our doped samples (Figures 5c & 6c). We see that the density of states effective mass does not vary with carrier concentration, suggesting the validity of the

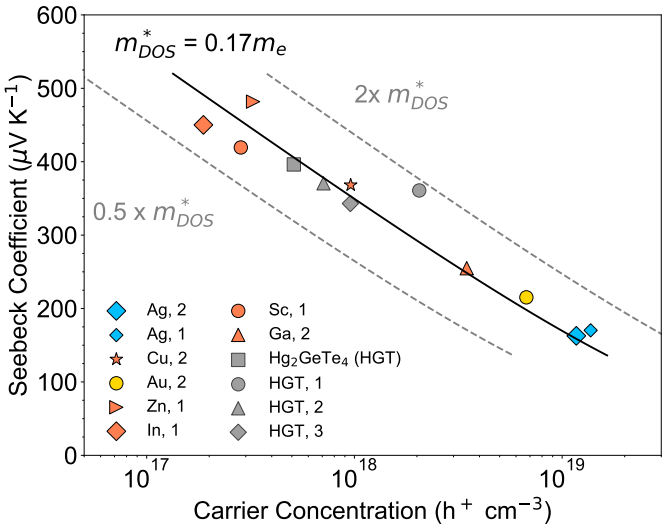

Fig. 4 To determine if doping induces any changes in effective mass, Seebeck coefficient and carrier concentration measurements were conducted at 50°C. Using the single parabolic band (SPB) approximation and the assumption of ionized impurity scattering, the SPB effective mass was tuned to fit the measured data. Numbers following dopant refer to chemical potential: 1 = Hg-rich/Ge-rich, 2 = Hg-poor/Ge-rich, 3 = Hg-rich/Ge-poor. Double and halved effective mass lines are shown for comparison.

rigid band approximation for doped Hg_2GeTe_4.

To understand how transport depends on temperature, we measured resistivity, Hall carrier concentration, and Seebeck coefficients on these samples from room temperature to 473K. The subsequent discussion follows the order presented in Figure 2c, and for Au and Ag, we consider the impact of the elemental chemical potentials on the efficacy of *p*-type doping.

2.2.1 Doping with Ag and Au

Hall carrier concentration Au and Ag are the best performing *p*-type dopants, with maximum carrier concentrations of 7.7 × 10^{18} h^+ cm^{-3} and 1.6 × 10^{19} h^+ cm^{-3}, respectively. Figure 5a shows that the experimental carrier concentrations exhibit little temperature dependence, suggesting an extrinsic regime for both dopants. These doping levels are remarkably consistent with our predictions from theory (Figure 2c). For comparison, undoped stoichiometric and Hg-poor/Ge-rich samples are shown in grey.

Chemical potential control of carrier concentration The small chemical potential window of stability for undoped Hg_2GeTe_4 leads to limited effects on carrier concentration from phase boundary mapping. However, we find that the carrier concentration varies by a factor of two depending on growth conditions for Au-doping, as seen in Table 2 and Figure 5a. Here, the predictions of maximum carrier concentration under Hg-poor/Ge-rich conditions are born out for Au. For Ag, we find that the relationship between composition and carrier concentration is complicated by the presence of the previously unreported Ag-containing quaternary compound (Figure S4). Ag-doping does not show a preference for Hg-rich/Ge-rich vs Hg-poor/Ge-rich conditions and high carrier concentration is achieved under both regimes (Table 2).

Seebeck coefficient The Seebeck coefficient data are largely linear with temperature, consistent with the extrinsic regime found in the Hall measurements. All Ag-doped samples possess higher carrier concentration and lower Seebeck coefficient than Au-doped material (Figure 5b), which reflects expected classical semiconductor behavior. Likewise, all Au and Ag samples show Seebeck coefficients that are suppressed compared to the undoped Hg_2GeTe_4. Resistivity values for Ag and Au doped Hg_2GeTe_4 range from 10 – 50 mΩ cm (Figure 5d), which is about an order of magnitude lower than the undoped range (150 – 400 mΩ cm). The decreased Seebeck and resistivity values for these samples reflect successful *p*-type doping that pushes the E_F towards the valence band edge.

Hall mobility Considering the Hall mobility μ of Ag and Au doped Hg_2GeTe_4, the absolute magnitudes are quite different (Figure 5c). Ag doping leads to low mobilities (15-45 cm^2 V^{-1} s^{-1}) whereas Au doped samples exhibit high mobilities (60-85 cm^2 V^{-1} s^{-1} at 323 K). This difference is a bit surprising, as they have similar defect energetics and chemistry. The following discussion considers the role of Hg vacancies as scattering centers, and how their varying concentrations in Ag vs Au-doped polycrystalline material could contribute to different mobility values.

Doping with Ag and Au moves the Fermi level towards the valence band edge, which increases the formation energy of native defect V_{Hg}^{-2} (Figure 3). In these doped samples, the extrinsic dopants form at high concentrations compared to the native Ge_{Hg}^{+2} (∼ 0.4 eV) and V_{Hg}^{-2} (∼1 eV) defects at the equilibrium Fermi level. As vacancies are efficient scattering centers, it is expected that the reduction in concentration of V_{Hg}^{-2} in doped material will increase the mobility. Indeed, in Figure 5c we generally observe higher mobility for doped vs undoped material at room temperature. At elevated temperature, undoped samples exhibit a strong rise in mobility with increasing temperature, a hallmark of ionized impurity scattering or grain boundary scattering[36,37]. In contrast, doped samples generally demonstrate evidence of phonon scattering i.e. a decay in mobility with temperature.[35,38] These observations suggest that the V_{Hg}^{-2} serve as strong scattering centers in undoped Hg_2GeTe_4 and their concentration is sufficiently high to dominate the mobility. Future work might consider a more in-depth study on the scattering limits to mobility in the doped system to understand why Au-doping results in such high mobility.

Thermoelectric figure of merit Doping with Ag results in the highest carrier concentration for Hg_2GeTe_4. All Ag-doped samples have similar carrier concentration around 1 × 10^{19} h^+ cm^{-3} at high temperature (Figure 5a),but the $Hg_{1.93}GeTe_4Ag_{0.07}$ sample has the highest high temperature Seebeck value and excellent electronic conductivity. As such, we measured the thermal conductivity of this sample from room temperature to 473 K as described in Methods. Its zT value is 0.40 (Figure 5e) and we see that is very close to the maximum zT predicted from the SPB model.

From the SPB model we calculated theoretical zT as a function

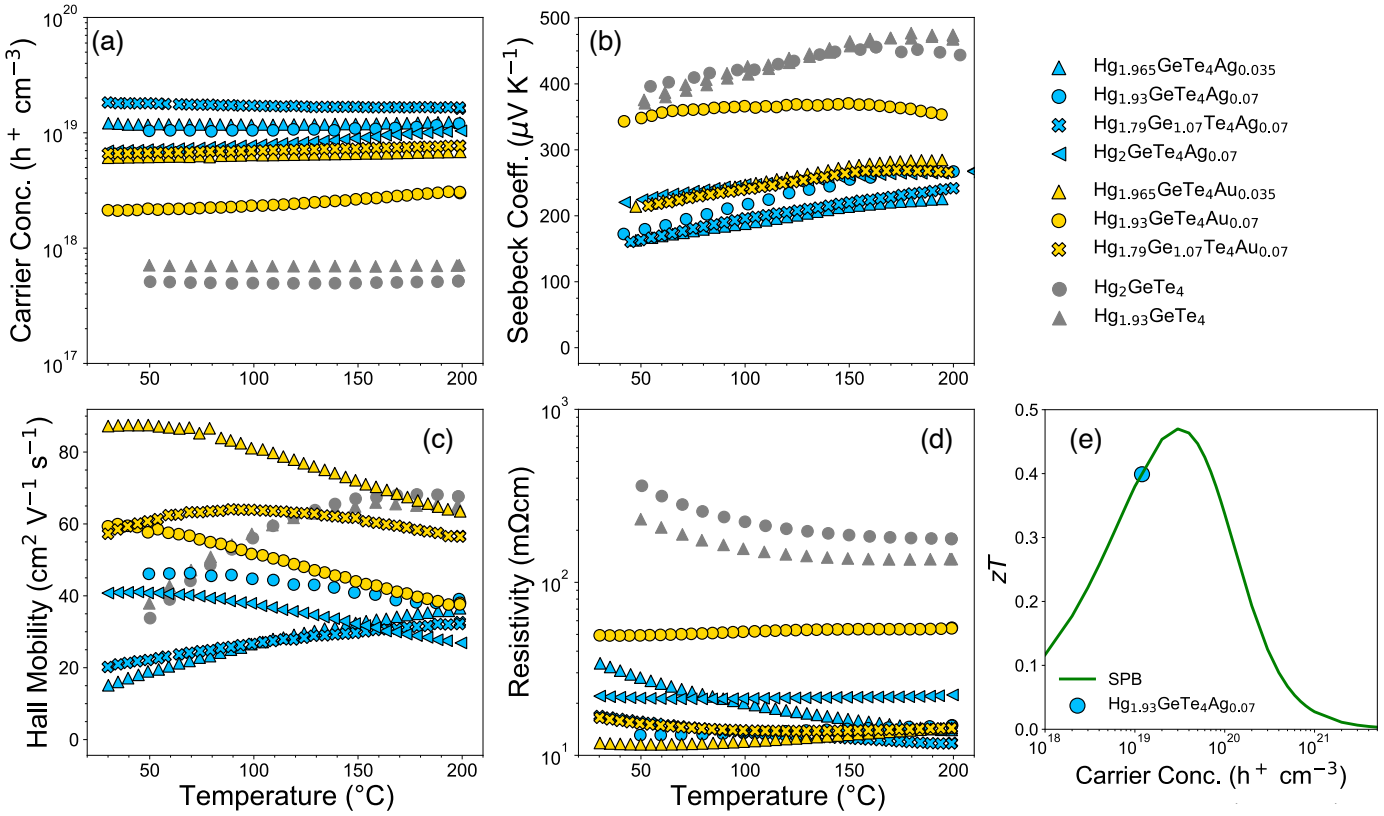

Fig. 5 The experimental high temperature transport properties of Hg_2GeTe_4 doped with Ag (blue) and Au (yellow) consistently demonstrate efficient *p*-type doping. Undoped stoichometric (grey circles) and Hg-poor/Ge-rich (grey triangles) samples are shown for reference. Panel (e) shows zT calculated from experimental data using an SPB model at 473K assuming acoustic phonon scattering. The experimental sample $Hg_{1.93}GeTe_4Ag_{0.07}$ is close to achieving the maximum possible *p*-type zT in Hg_2GeTe_4.

of carrier concentration under the following assumptions: we are in a regime where conduction from minority carriers is negligible, the dominant scattering mechanism is acoustic phonon scattering (r = –0.5), and the *DOS* effective mass m^*_{DOS} is 0.86m_e as determined from the experimental carrier concentration at 473 K also using the SPB model.[35] We note that this is a different scattering mechanism than we used in the generation of our Pisarenko plot (Figure 4), because ionized impurity scattering is dominant at lower temperatures and at higher temperatures (Figure 5e is at 473 K) the mobility is limited by acoustic phonon scattering. This model shows us that our efforts are very close to the maximum possible zT for our system: 0.5, which could be reached at 3.0 × 10^{19} h^+ cm^{-3} (Figure 5e). Our achieved zT value of 0.4 is higher than other diamond-like semiconductor materials at this relatively low temperature[39,40] and we conclude that our *p*-type doping efforts were quite successful.

2.3 Doping with Cu

At dilute doping levels (Table 2), Cu appears to be ineffective at driving large changes to the carrier concentration of Hg_2GeTe_4. Temperature-dependent measurements of Hall, resistivity, and Seebeck coefficients for Cu-doped samples fall within the range of undoped material (Figure S6). This is consistent with the calculations discussed above, where Cu was found to be heavily compensated between Cu^{-1}_{Hg} and Cu^{+1}_{i}. We note that $Hg_{2-x}Cu_{2x}GeTe_4$ forms a full solid solution ($0 \leq x \leq 1$) and at high Cu concentrations when the carrier concentration is greater than 10^{21} h^+ cm^{-3}.[18] However, these effects are not seen until dopant levels far beyond the dilute limit approximation of the defect calculations herein and a change in lattice symmetry follows the increase in Cu content.[18,23]

2.3.1 Compensated dopants: In, Sc, Zn, Ga

Doping with In, Sc and Zn reduced the carrier concentration of Hg_2GeTe_4 by one order of magnitude from native Hg-rich/Ge-rich levels, as seen in Figure 6a. Ga-doping resulted in either *p*-type or bipolar Hall transport depending on the growth condition (Table 2), and these transport data are shown in Figure S5. When Hg-rich/Ge-rich, the native carrier concentration of Hg_2GeTe_4 is 1 – 2 × 10^{18} h^+ cm^{-3}, and doped carrier concentration with In, Sc and Zn across the measured temperature range in Figure 6a is 2 – 3 × 10^{17} h^+ cm^{-3}. This reduction in carrier concentration while remaining *p*-type suggests that we have moved the Fermi level more midgap, without fully pushing it to the conduction band. Compared to the dopant calculations discussed above, we find that the shift in the Fermi level arising from doping is approximately half that of the predicted value.

Further evidence of shifting the Fermi level midgap is our measured high resistivity and Seebeck coefficient values. Room tem-

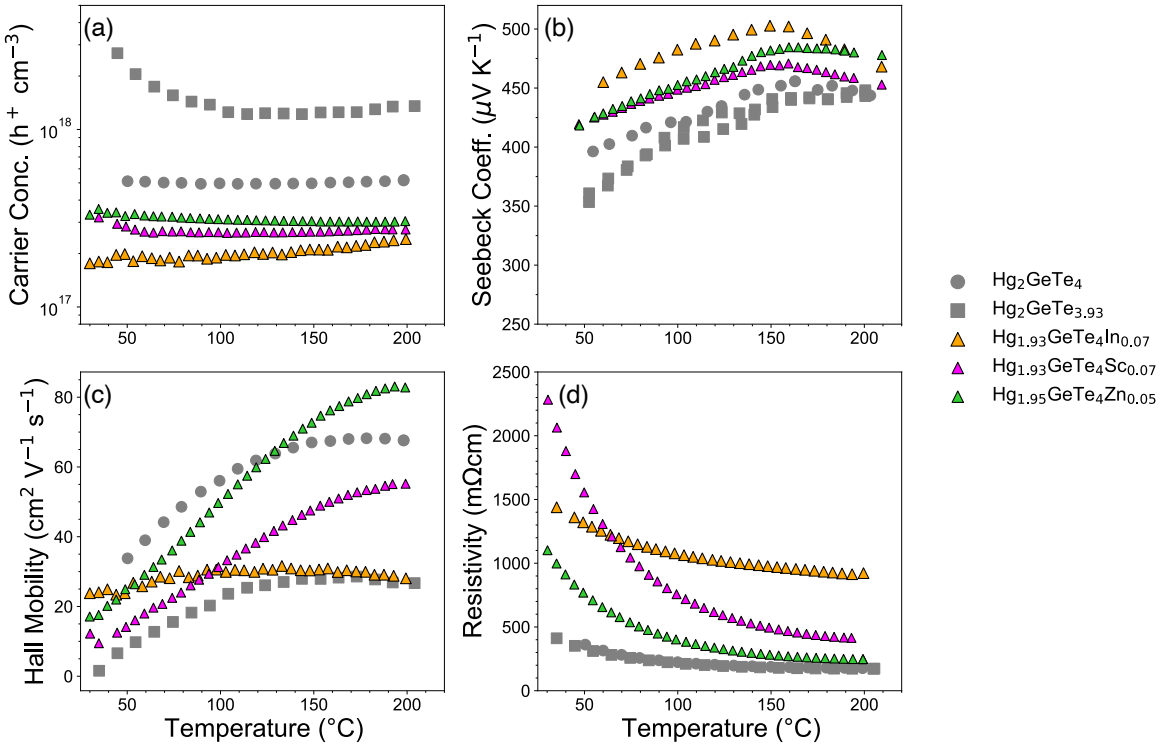

Fig. 6 The experimental transport data for samples doped with In, Sc, and Zn demonstrate that these dopants push the Fermi level midgap relative to the undoped compound (grey circles; grey squares designate a native Hg-rich/Ge-rich sample): (a) the carrier concentration is decreased from undoped levels, (b) the Seebeck coefficient is increased, and (d) the resistivity is more than double undoped levels at room temperature. The temperature dependence of the mobility in panel (c) indicates that ionized defect scattering is significant in these samples.

perature resistivity is two to sixfold higher than undoped resistivity for samples doped with Zn, Sc, and In (Figure 6d). Correspondingly, Seebeck values are significantly higher than undoped Hg_2GeTe_4 (Figure 6b). While resistivity drops with increasing temperature for Zn and Sc (Figure 6d), it holds steady with temperature for indium. Calculating the band gap of Hg_2GeTe_4 from the resistivity the Arrhenius method does not yield results consistent with DFT calculations (E_{gap} (DFT) = 0.48 eV[5]; E_{gap} (from measured resistivity, Arrhenius) = 0.070 – 0.30 eV). Instead, the temperature-dependence of the resistivity is driven by the hole mobility. Much like undoped Hg_2GeTe_4, the mobility rises sharply with increasing temperature for the Zn and Sc-doped samples (Figure 6c). We associate this behavior with the high concentration of V_{Hg}^{-2} in these samples arising from shifting the Fermi level towards the conduction band. Additionally, this rise in mobility could be due to grain boundary scattering. In-doping retains low mobility, suggesting strong charge carrier scattering at all temperatures.

Conclusion

In this work, we surveyed 16 extrinsic dopants for their ability to tune the carrier concentration of ordered vacancy compound Hg_2GeTe_4 by introducing low energy extrinsic defects. We found from first-principles calculations that 8 of the 16 dopants are successful at tuning the carrier concentration of Hg_2GeTe_4, and we synthesized samples with 7 of these dopants (avoiding Li due to its reactivity and potential to form Li-Hg compounds). The best predicted dopants are Ag and Au and they achieve the highest carrier concentrations experimentally: Ag and Au reach maximum carrier concentrations of 1.6×10^{19} h^+ cm^{-3} and 7.7×10^{18} h^+ cm^{-3} respectively, which are over an order of magnitude above undoped levels. Our best thermoelectric performance is realized via Ag-doping, and at 473 K zT = 0.4. Additionally, dopants predicted to minimally impact the carrier concentration (Cu) or decrease the carrier concentration (Sc, Zn, In) are confirmed through experiment. Identifying successful dopants to improve the electronic properties of complex semiconductors can be rapidly accelerated through computation-guided experiment. This study serves as a successful case study in such collaborations, which will be increasingly necessary as an ever-growing number of complex materials require optimization of their electronic properties.

Methods

2.4 Computational

Structure relaxation and phase stability

First-principles density functional theory (DFT) calculations were performed using the Vienna *Ab initio* Simulation Package (VASP)[41]. We used projector-augmented wave (PAW)[42] pseudopotentials to represent core electrons. The plane-wave energy cutoff was set to 400 eV for all calculations. The Heyd-Scuseria-Ernzerhof[43] (HSE06) hybrid exchange correlation functional was used with an exchange mixing of α = 0.25. During structural

relaxation, the convergence criteria for energy and forces relaxations are set as 10^{-5} eV and 10^{-4} eV Å^{-1}, respectively. An automatically generated $2 \times 2 \times 2$ Γ-centered regular k-point mesh was used to sample the Brillouin zone.

Native and Extrinsic Defect Energetics

For defect chemistry, we adopted the standard supercell approach[44] to calculate defect formation energies of native and extrinsic point defects. A $2 \times 2 \times 2$ supercell of Hg_2GeTe_4, containing 56 atoms, was considered for all defect formation energy calculations. All native point defects were calculated in charge states ranging from –3 to +3. The defect formation energy ($\Delta E_{D,q}$) for a defect D in charge state q was calculated from supercell total energies according to the formula:

$$\Delta E_{D,q} = E_{D,q} - E_{\text{host}} + \sum_i n_i \mu_i + q E_F + E_{\text{corr}} \quad (3)$$

where $\Delta E_{D,q}$ is the formation energy of a defect D in charge state q, $E_{D,q}$ and E_{host} correspond to the total energies of the supercell with and without the defects, respectively. E_F represents for Fermi energy, ranging from the valence band maximum (VBM) to the conduction band minimum (CBM). μ_i is the chemical potential of elemental species i added ($n_i < 0$) or removed ($n_i > 0$) from the host supercell to form defects. The elemental chemical potential μ_i is expressed relative to a reference state (μ_i^0) and defined as $\mu_i = \mu_i^0 + \Delta\mu_i$, where μ_i^0 is the reference elemental potential obtained from structure relaxations of bulk elements and $\Delta\mu_i$ the deviation from the reference elemental phase. The bounds on $\Delta\mu_i$ are set by ta set of thermodynamic stability conditions; specifically, $\Delta\mu_i$ should follow the constraint $2\Delta\mu_{Hg} + \Delta\mu_{Ge} + 4\Delta\mu_{Te} = \Delta H_f^{Hg2GeTe4}$, where $\Delta H_f^{Hg2GeTe4}$ is the formation enthalpy of the main compound Hg_2GeTe_4. Also, $\Delta\mu_{Hg}$, $\Delta\mu_{Ge}$, and $\Delta\mu_{Te}$ values should satisfy the constraint that other competing phases are unstable relative to Hg_2GeTe_4. In experiments, $\Delta\mu_i = 0$ corresponding to i-rich conditions and a large negative value of $\Delta\mu_i$ represents i-poor growth conditions.

Due to the presence of heavy elements Hg and Te, the band edge position has been corrected by consideration of spin-orbit coupling (SOC) effects. We applied band edge shifts by comparing the average electrostatic potential to match calculations from HSE06+SOC. The predicted band gap from HSE06+SOC calculations is shown in the defect diagrams.

To account for the finite-size corrections within the supercell approach, E_{corr} is added as an additional correction term following the methodology of Lany and Zunger[44]. The finite-size corrections include: (i) potential alignment correction to account for the misalignment of the average electrostatic potential between the neutral, defect-free host supercell and the charged, defected supercells, (ii) image charge correction to describe the long-range electrostatic interactions between charged defects and its periodic defect images, and (iii) band-filing corrections for Moss-Burnstein-type filling in shallow defects.

We consider that dopants can occupy the Hg, Ge, or Te site. Formation of interstitials is also possible. The possible intersitial sites were determined by a Voronoi tessellation scheme implemented in *pylada-defects*[45]. We considered 10-15 possible interstitial defects and determined the lowest energy interstitial site by total energies of the relaxed supercells. Only the lowest energy defects with $\Delta E_{D,q} < 0.5$ eV are shown in the defect diagrams.

Defect and carrier concentrations

The free carrier concentrations were calculated by solving the charge-neutrality condition ($\sum qC_{D,q} - n + p = 0$) at specific temperatures. The carrier concentration can then be analytically approximated as:

$$n \approx 2\left[\frac{2\pi m_e^* k_B T}{h^2}\right]^{3/2} \exp\left(\frac{E_F - E_{CBM}}{k_B T}\right) \quad (4)$$

$$p \approx 2\left[\frac{2\pi m_h^* k_B T}{h^2}\right]^{3/2} \exp\left(\frac{E_{VBM} - E_F}{k_B T}\right) \quad (5)$$

While screening for dopants, we allowed each element to adopt all possible charge states (q = -6 to +6) and positions within the lattice while sampling across the available chemical potential range. This agnosticism to a dopant's role as a donor or acceptor (or both) allowed for a single dopant to act as n- or p-type under different synthetic growth conditions and avoided any potential bias that could be introduced by our chemical intuition.

2.5 Experimental

Synthesis

Samples were prepared from elemental precursors of high purity (Hg, liquid, Alfa 99.999%, Ge, ingot, Indium Corp. 99.999%, Te, ingot 5NPlus Inc. 99.999%) under solid state reaction methods. Elements were weighed in air to yield about 10g total of the stoichiometric ratios given in Table 2. Each sample batch was ball milled in an inert nitrogen environment for 90 minutes, rotating the vial once at the 45 minute mark. After ball milling, the powder was hand ground with an agate mortar and pestle, loaded into a clean quartz ampoule, and evacuated and sealed using a vacuum pump and torch. Sealed ampoules containing the sample were annealed at 350°C for 72 hours, and allowed to cool slowly to promote the sample achieving equilibrium. Cooled ampoules were broken open, the ingot was extracted, and powder was hand ground and passed through a 200 mesh sieve, all in air. Three grams of the resulting powder were loaded into a graphite die and hot pressed under vacuum at 330°C for at least 6 hours to form a consolidated pellet. Pellets were polished to a flatness of +/- 5 μm for measurements.

For Au and Sc doped samples, a 900°C melt for 12 hrs followed by a gradual cool was performed before ball milling to incorporate the dopant with Te, forming a binary telluride compound that could be subsequently ball milled to form Hg_2GeTe_4. Without this preliminary melt step, the dopant remains elemental and either gums up (Au), or is too tough in its elemental form (Sc) to incorporate.

Characterization

All samples underwent X-ray diffraction (XRD), scanning electron microscopy, and energy dispersive spectroscopy (SEM/EDS) to confirm excellent sample quality and to determine competing phases present. XRD data were collected on a Bruker D2 phaser

diffractometer in $\theta - 2\theta$ mode from 10 – 80° of 2θ and analyzed with data from the Inorganic Crystal Structure Database (ICSD) for Hg_2GeTe_4 and all competing phases. Rietveld analysis was performed using the TOPAS Academic v6 software[29] and phases as well as lattice parameters were refined. SEM and EDS were performed on a FEI Quanta 600i SEM. A minimum of five locations across each phase present were probed using EDS for each sample to determine the identify of a particular phase.

Electronic and thermal transport measurement

Resistivity and Hall data were measured on an in-house custom built instrument[46] from 50–200°C under vacuum. Seebeck data were also gathered on a custom built instrument[47] over the same temperature range, under an inert N_2 environment. All samples underwent at least two heating and cooling cycles to verify that no sample evolution was occurring over the course of the measurement. Thermal diffusivity was measured on a Netzsch Laser Flash Apparatus (LFA) 457. The heat capacity was estimated using the Dulong–Petit approximation to calculate the thermal conductivity of the sample. The Lorenz number was calculated from the SPB model using experimental Seebeck data as input.[35]

Author Contributions

CEP and JQ contributed equally to project conceptualization, investigation, visualization, formal analysis, and writing - original draft. JQ was responsible for computational methodology and CEP was responsible for experimental methodology. KC contributed writing - review & editing, and formal analysis of transport data. EST and EE contributed project administration, conceptualization, and writing - review & editing.

Conflicts of Interest

There are no conflicts of interest to declare.

Acknowledgements

This work was funded primarily with support from the U.S. National Science Foundation (NSF) via Grant No. DMR 1729149 and DMR 1729594. J.Q. and E.E. acknowledge funding from NSF DIGI-MAT program, Grant No. 1922758. This work used the Extreme Science and Engineering Discovery Environment (XSEDE) Bridges-2 at the Pittsburgh Supercomputing Center through allocation TG-MAT220011P. This research is also part of the Blue Waters sustained-petascale computing project, which is supported by the National Science Foundation (awards OCI-0725070 and ACI-1238993) the State of Illinois, and as of December, 2019, the National Geospatial-Intelligence Agency. Blue Waters is a joint effort of the University of Illinois at Urbana-Champaign and its National Center for Supercomputing Applications.

References

1 X. Ma, L. Yang, K. Lei, S. Zheng, C. Chen and H. Song, *Nano Energy*, 2020, **78**, 105354.
2 M. Chan, S. Lai, M. Fung, C. Lee and S. Lee, *Applied physics letters*, 2007, **90**, 023504.
3 F. Demichelis, C. Pirri and E. Tresso, *Journal of Applied Physics*, 1992, **72**, 1327–1333.
4 J. He and T. M. Tritt, *Science*, 2017, **357**, 1.
5 J. Qu, C. E. Porter, L. C. Gomes, J. M. Adamczyk, M. Y. Toriyama, B. R. Ortiz, E. S. Toberer and E. Ertekin, *Journal of Materials Chemistry A*, 2021, **9**, 26189–26201.
6 A. Polman, M. Knight, E. C. Garnett, B. Ehrler and W. C. Sinke, *Science*, 2016, **352**, aad4424.
7 G. J. Snyder and E. S. Toberer, *Nature materials*, 2008, **7**, 105–114.
8 J. Maier, *Journal of The Electrochemical Society*, 2015, **162**, A2380.
9 Y.-Y. Lin, J. Qu, W. J. Gustafson, P.-C. Kung, N. Shah, S. Shrivastav, E. Ertekin, J. A. Krogstad and N. H. Perry, *Journal of Power Sources*, 2023, **553**, 232251.
10 W. Xiao, J. Wang, X. Zhao, J. Wang, G. Huang, L. Cheng, L. Jiang and L. Wang, *Solar Energy*, 2015, **116**, 125–132.
11 C. G. Van de Walle and J. Neugebauer, *Journal of applied physics*, 2004, **95**, 3851–3879.
12 P. Gorai, V. Stevanović and E. S. Toberer, *Nature Reviews Materials*, 2017, **2**, 1–16.
13 Y. Zheng, T. J. Slade, L. Hu, X. Y. Tan, Y. Luo, Z.-Z. Luo, J. Xu, Q. Yan and M. G. Kanatzidis, *Chemical Society Reviews*, 2021.
14 P. Xu, Y. Sun, C. Shi, F. Xu and H. Pan, *Nuclear Instruments and Methods in Physics Research Section B: Beam Interactions with Materials and Atoms*, 2003, **199**, 286–290.
15 S. Zhang, S.-H. Wei, A. Zunger and H. Katayama-Yoshida, *Physical Review B*, 1998, **57**, 9642.
16 B. R. Ortiz, P. Gorai, V. Stevanovic and E. S. Toberer, *Chemistry of Materials*, 2017, **29**, 4523–4534.
17 S. Ohno, K. Imasato, S. Anand, H. Tamaki, S. D. Kang, P. Gorai, H. K. Sato, E. S. Toberer, T. Kanno and G. J. Snyder, *Joule*, 2018, **2**, 141–154.
18 B. R. Ortiz, K. Gordiz, L. C. Gomes, T. Braden, J. M. Adamczyk, J. Qu, E. Ertekin and E. S. Toberer, *Journal of materials chemistry A*, 2019, **7**, 621–631.
19 J. M. Adamczyk, L. C. Gomes, J. Qu, G. A. Rome, S. M. Baumann, E. Ertekin and E. S. Toberer, *Chemistry of Materials*, 2020.
20 J. H. Werner, J. Mattheis and U. Rau, *Thin Solid Films*, 2005, **480**, 399–409.
21 P. Kumar, J. Sahariya, A. Soni and K. Bhamu, Materials Science Forum, 2017, pp. 69–73.
22 S. A. Miller, M. Dylla, S. Anand, K. Gordiz, G. J. Snyder and E. S. Toberer, *npj Computational Materials*, 2018, **4**, 1–8.
23 B. L. Levy-Wendt, B. R. Ortiz, L. C. Gomes, K. H. Stone, D. Passarello, E. Ertekin, E. S. Toberer, M. F. Toney, D. Collaboration *et al.*, *Physical Review Materials*, 2021, **5**, 015402.
24 J.-H. Yang, W.-J. Yin, J.-S. Park and S.-H. Wei, *Scientific reports*, 2015, **5**, 16977.
25 J. Woolley and B. Ray, *Journal of Physics and Chemistry of Solids*, 1960, **13**, 151–153.
26 A. Marbeuf, R. Druilhe, R. Triboulet and G. Patriarche, *Journal of crystal growth*, 1992, **117**, 10–15.
27 S. Zhang, S. Xu, H. Gao, Q. Lu, T. Lin, P. He and H. Geng, *Journal of Alloys and Compounds*, 2020, **814**, 152272.

28 H. Okamoto, T. Massalski *et al.*, *ASM International, Materials Park, OH, USA*, 1990, 12.

29 A. A. Coelho, *Journal of Applied Crystallography*, 2018, **51**, 210–218.

30 M. Kretova, E. Avilov and M. Korzhuev, *Russian Metallurgy (Metally)*, 2020, **2020**, 387–395.

31 D. Weitze and V. Leute, *Journal of Alloys and Compounds*, 1996, **236**, 229–235.

32 V. Leute, D. Weitze and A. Zeppenfeld, *Journal of alloys and compounds*, 1999, **289**, 233–243.

33 N. K. Abrikosov, G. Danilova-Dobryakova and R. Shalamberidze, *Izvestiya Akademii Nauk SSSR, Neorganicheskie Materialy*, 1976, **12**, 605–609.

34 M. Markov, X. Hu, H.-C. Liu, N. Liu, S. J. Poon, K. Esfarjani and M. Zebarjadi, *Scientific reports*, 2018, **8**, 1–10.

35 D. M. Rowe, *CRC handbook of thermoelectrics*, CRC press, 2018.

36 Z. Han, J.-W. Li, F. Jiang, J. Xia, B.-P. Zhang, J.-F. Li and W. Liu, *Journal of Materiomics*, 2022, **8**, 427–436.

37 K. Imasato, C. Fu, Y. Pan, M. Wood, J. J. Kuo, C. Felser and G. J. Snyder, *Advanced Materials*, 2020, **32**, 1908218.

38 K. Ahn, C.-P. Li, C. Uher and M. G. Kanatzidis, *Chemistry of Materials*, 2010, **22**, 876–882.

39 J. Fan, H. Liu, X. Shi, S. Bai, X. Shi and L. Chen, *Acta materialia*, 2013, **61**, 4297–4304.

40 R. Liu, L. Xi, H. Liu, X. Shi, W. Zhang and L. Chen, *Chemical Communications*, 2012, **48**, 3818–3820.

41 G. Kresse and J. Furthmüller, *Phys. Rev. B*, 1996, **54**, 11169.

42 P. E. Blöchl, *Phys. Rev. B*, 1994, **50**, 17953.

43 A. V. Krukau, O. A. Vydrov, A. F. Izmaylov and G. E. Scuseria, *The Journal of chemical physics*, 2006, **125**, 224106.

44 S. Lany and A. Zunger, *Phys. Rev. B*, 2008, **78**, 235104.

45 A. Goyal, P. Gorai, H. Peng, S. Lany and V. Stevanovic, *Comput. Mater. Sci.*, 2017, **130**, 1.

46 K. A. Borup, E. S. Toberer, L. D. Zoltan, G. Nakatsukasa, M. Errico, J.-P. Fleurial, B. B. Iversen and G. J. Snyder, *Review of Scientific Instruments*, 2012, **83**, 123902.

47 S. Iwanaga, E. S. Toberer, A. LaLonde and G. J. Snyder, *Review of Scientific Instruments*, 2011, **82**, 063905.